

Simulating the influence of stoichiometry on the spectral emissivity of Mo_xSi_y thin films

Zahra Golsanamlou,^{*} Arseniy Baskakov, Robbert van de Kruijs, Marcelo Ackermann, and Menno Bokdam[†]
*University of Twente, Faculty of Science and Technology and MESA+ Institute for Nanotechnology,
P.O. Box 217, 7500 AE Enschede, the Netherlands*

Silvester Houweling and Giorgio Colombi
ASML Research, Materials and Chemistry, 5504 DT Veldhoven, the Netherlands
(Dated: March 19, 2026)

In this work, we simulate the spectral emissivity of various stoichiometric crystal phases of Mo_xSi_y compounds using density functional perturbation theory. The dielectric function, including electronic and ionic contributions, is calculated for each phase. We use the bulk properties obtained to simulate the optical absorption spectrum originating from the compound in thin film (~ 20 nm) form. We find that most thin films of Mo_xSi_y are metallic, however, our results indicate that their emissivity is not simply correlated with the Mo content. For hot metallic films at around 900 K, we predict a maximal emissivity between 5-10 nm thickness. Our results are in good qualitative agreement with experiments, confirming that the emissivity of hexagonal MoSi_2 is much lower than in the tetragonal phase. This is related to the small band gap (hexagonal MoSi_2) and low density of states at the Fermi level (tetragonal MoSi_2). Furthermore, test calculations on defected MoSi_2 demonstrate that the infrared emissivity of MoSi_2 thin films can be substantially increased by introducing defects.

I. INTRODUCTION

Materials that can withstand high temperatures for a long period of time are of increasing scientific and technological importance[1–3]. Especially when used as coatings or thin films, their physical and chemical properties on an atomistic scale are important. To prevent overheating, breaking, or melting, a thermal balance has to be established between external heating and cooling of the film. The film can be cooled by thermal conduction to a heat sink, or by passive radiative cooling. The larger open question is how the atomic structure (i.e., crystallinity and defects) of the thin film controls its heat management. Here, we focus on the effect of atomic composition and structure on the dielectric properties of the film. The passive radiative cooling ability of a thin film is expressed by its emissivity; a temperature-dependent quantity with a value between zero and one. An emissivity of one means that the thin film has the same radiative capacity as a black body radiator at temperature T , and zero means that at this temperature the film is incapable of emitting any radiation. Film thickness is an important parameter for emissivity. The emissivity of dielectric films decreases with the thickness of the film. For metallic films, the emissivity is constant, but when film-thickness reduces to the order of tens of nanometers, the emissivity suddenly increases as a result of multiple reflections in the thin film[4]. In this work, we focus on thermal radiation for the case of optically thin films, which means that their thickness is less than the typical

penetration depth (also known as skin depth) of the incoming light. We present results from a first-principles based modeling study of thin film emissivity. The presented materials modeling scheme is general, and can aid with the phenomenological interpretation of the experimental observations by simulating the effect of changing atomic structure. We apply the scheme to the case study of Mo_xSi_y , as our study has been carried out in parallel to recent ellipsometry measurements of $\text{Mo}_x\text{Si}_{1-x}$ thin films by Baskakov *et al.*[5]. Their crystallographic and spectroscopic measurements on sputter-deposited films point towards the importance of crystal phases and electronic structure (band structure and density of states at the Fermi level) combined with the concentration of metal (Mo) in the film.

Mo_xSi_y is an interesting, and technologically relevant, class of (polymorphous) thin film materials that can become metallic or semiconducting depending on the stoichiometry. Different crystal phases of Mo_xSi_y are reported in the Materials Project data base[6, 7], but only a subset of those have been observed in diffraction experiments (Mo, Mo_3Si , Mo_5Si_3 , MoSi_2 , and Si)[8, 9]. Crystal structures related to stoichiometries such as MoSi_3 , MoSi and Mo_3Si_2 are not thermodynamically stable and phase segregate in stable (poly)-crystalline domains[10]. Mo_xSi_y -based materials have elevated melting points, suitable thermal and electrical conductivity, low molecular density and high oxidation resistance, making them suitable for high temperature applications [3, 11–17]. Their melting temperature (T_m) increases with the atomic fraction of Mo ($\frac{x}{x+y}$), starting at 1687 K for pure Si, increasing to 2293 K for MoSi_2 , and further to 2453 K for Mo_5Si_3 , upon reaching 2896 K for pure Mo[10, 18]. Mo_xSi_y -based materials are currently being explored for a range of applications, including

^{*} z.golsanamlou@dynamicssolids.net

[†] m.bokdam@utwente.nl

turbine airfoils, diesel engine glow plugs, combustion chamber components in oxidizing environments, industrial gas burners, molten metal lances, glass processing materials [9, 19] and extreme ultraviolet (EUV) pellicle applications[20, 21]. Tetragonal MoSi₂ could specifically be an attractive candidate for display devices, ultraviolet (UV) absorbers, and to prevent solar heating[22]. For these kinds of applications, thin films of the material are preferred.

Some experimental and theoretical works have already been performed on the emissivity of Mo_xSi_y-based compounds. Zheng *et al.*, explored experimentally the potential of pressureless sintered SiC-MoSi₂ composites for bulk infrared source applications[23]. They studied the effects of microstructure by increasing the sintering temperature and showed that this results in a decrease of the electrical resistivity and an increase in infrared emissivity. The very recent experimental investigation of Baskakov *et al.* on the emissivity of Mo_xSi_{1-x} films found that, the emissivity of 20 nm films that were annealed at 600 or 900 °C show considerably different emissivities. After annealing at 600°C, emissivities between 0.1 and 0.3 are reported for films with Mo content between 17 and 33 at.%. Annealing at a temperature of 900 °C results in a relative emissivity increase between 10 and 70%, however not increasing beyond 0.33. They concluded that these differences are related to the crystal phase present in the film, either hexagonal or tetragonal MoSi₂.

Previous simulation studies have shown that dielectric and optical properties are related to stoichiometry and crystal structure[24, 25] or quantum confinement[26]. To date, the emissivity of MoSi₂-based compounds has been sparsely investigated with theoretical approaches. Xiang *et al.* calculated the intrinsic electronic emissivity of tetragonal MoSi₂ as 0.17 at 300 K which increases to 0.51 at 1400 K[27]. To increase emissivity, they proposed a change of microstructure by incorporating grains of SiO₂. Liton *et al.* investigated the influence of hydrostatic pressure on the optical and thermal properties of tetragonal MoSi₂[22]. Song *et al.* investigated the effect of mixing in medium and high-entropy transition metal disilicides on emissivity[28].

Apart from MoSi₂, the emissivity of thin film Mo_xSi_y in other ($\frac{x}{x+y}$) stoichiometric ratios and correspondingly different crystal phases is not well-reported in the literature. In addition, the contribution of the vibrations of the ionic lattice to the dielectric response of the materials, and hence the emissivity, has not been calculated. Therefore, we here explore the emissivity of thin film Mo_xSi_y using first-principles and optical methods; including both electronic and ionic contributions, and allowing for multiple reflections within the thin film. A macroscopic optical model is used to simulate the effect of the extrinsic properties, such as film thickness and refractive index of the environment, on the emissivity of the thin film. We characterize the emissivity according to the electronic structure, and we compare the emissivity across material stoichiometry. Finally, we study the

effect of structural defects on the emissivity by supercell calculations of MoSi₂ test systems.

II. COMPUTATIONAL METHODS

A flowchart of our simulation approach is drawn in Figure 1. We start with a calculation of the electronic structure at the level of the bulk crystal. The resulting dielectric functions are passed on to calculate the absorption and emissivity of the material at the level of the thin film. In the following two subsections, we elaborate, in order of appearance from top to bottom, on the various methods in the flowchart.

A. Bulk crystal

The first-principles calculations presented in this work are based on Density Functional Theory (DFT). We consider several different crystal phases of Mo_xSi_y and optimize the related geometries until the total energy change between successive iterations is below 10⁻⁶ eV. The DFT calculations are performed using the Projector Augmented Wave (PAW) method[29] as implemented in the Vienna Ab-initio Simulation Package (VASP)[30–32] using a plane-wave basis with a cutoff of 520 eV. The generalized gradient approximation (GGA) of PBEsol[33] is used as the exchange-correlation

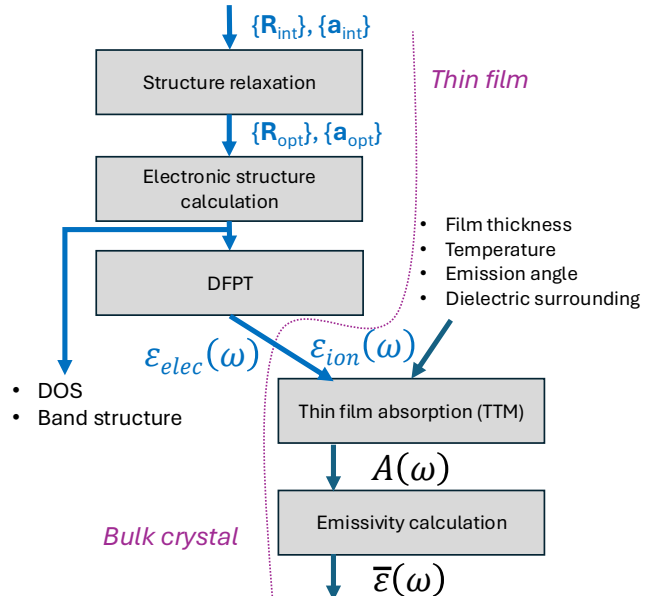


FIG. 1. Flowchart of the simulation and computation setup to calculate the emissivity of thin films starting from first principles. The input is formed by the atomic coordinates $\{\mathbf{R}_{1\dots N}\}$ and lattice vectors $\{\mathbf{a}_{1,2,3}\}$ of the structures in Figure 2. The purple dotted line divides the chart, the left hand is on the level of bulk crystal and the right hand side on the level of the thin film.

functional. The Brillouin zone integration is performed on Γ -centered Monkhorst-Pack k-point meshes, and a Gaussian smearing width of $\sigma = 0.2$ eV broadens the one-electron levels. The same σ value is used for all materials and corresponds to a relatively high temperature broadening. For density of states (DOS) calculations, the tetrahedron method is used on the final relaxed structures. A $18 \times 18 \times 6$ k-point mesh is used to sample the Brillouin zone of tetragonal MoSi₂. For the other Mo_xSi_y structures k-point meshes of similar density are used, taking into account their respective lengths of the lattice vectors and thereby creating the mesh with the closest matching k-point sampling density to that of MoSi₂.

The dielectric function is modeled as the addition of independent terms on a common frequency grid

$$\begin{aligned} \varepsilon(\omega) &= \varepsilon_{\text{elec.}}(\omega) + \varepsilon_{\text{ion}}(\omega) \\ &= \underbrace{\varepsilon_{\text{inter}}(\omega) + \varepsilon_{\text{intra}}(\omega)} + \varepsilon_{\text{ion}}(\omega). \end{aligned} \quad (1)$$

We create an isotropic solution by averaging the diagonal of the dielectric tensor $\varepsilon_{\alpha\beta}(\omega)$, where α, β are the Cartesian directions. For the electronic part, we distinguish between inter- and intra-band contributions. The inter contribution is calculated using Density Functional Perturbation Theory (DFPT) within the density-density picture[34–36]. For intrinsic semiconductors and insulators, all valence bands are fully occupied and (small) excitations inside the band cannot be made, resulting in an intra-band contribution of zero. For metals and doped or small band gap semiconductors at finite temperatures, the intra-band transitions can be described by a free-electron plasma (Drude) model, where the dielectric function is parameterized by the plasma frequency (ω_p) and a damping factor (γ)[37, 38]. The intra-band dielectric function composed of real and imaginary parts is then written as[24]

$$\varepsilon_{\text{intra}}(\omega) = \varepsilon_{\infty} - \frac{\omega_p^2}{\omega^2 + \gamma^2} + \frac{\gamma\omega_p^2}{\omega^3 + \omega\gamma^2}i, \quad (2)$$

where the constant ε_{∞} describes the screening by electronic inter-band transitions. In a pure Drude metal ε_{∞} is the vacuum permittivity of 1, but in the Mo_xSi_y materials there are inter-band transitions making $\varepsilon_{\infty} = \lim_{\omega \rightarrow 0} \varepsilon_{\text{inter}}(\omega)$. When adding the intra-contribution to the common grid (Eq. 1) we set ε_{∞} in Eq. 2 to zero in order to prevent double counting the vacuum permittivity. The plasma frequencies are computed for the eight crystalline structures in this study based on the full DFT calculated electronic dispersion near the Fermi level. In Supplementary Material (SM) [39] Section 1, the calculation method for ω_p and its dependence on sufficiently dense k-point grids and the applied smearing width, is discussed. The damping factor is treated as a parameter. Throughout, a value of $\gamma = 0.15$ eV is set, which is between the values obtained in experiment[5], and is a

typical value for metals. For the ionic part, the contributions are computed using the $\mathbf{q} = 0$ harmonic phonon modes and the Born effective charge tensors, as implemented in VASP[40].

B. Thin film

The optical penetration depth (d_{pen}) is a measure of how far light can penetrate inside a material. We use it to assess whether multiple reflections inside the thin film are to be expected, i.e., when the film thickness $d \leq d_{\text{pen}}$. The penetration depth is calculated as

$$d_{\text{pen}} = \frac{\lambda(\omega)}{4\pi k(\omega)}, \quad (3)$$

where the wavelength of the incoming light $\lambda(\omega)$ is expressed in nm and $k(\omega)$ is the extinction coefficient. Both the refractive coefficient $n(\omega)$ and the extinction coefficient $k(\omega)$ are calculated from the real/complex parts of the bulk dielectric function $\varepsilon(\omega) = \varepsilon'(\omega) + i\varepsilon''(\omega)$ as follows

$$\begin{aligned} n(\omega) &= \sqrt{\frac{|\varepsilon(\omega)| + \varepsilon'(\omega)}{2}} \\ k(\omega) &= \sqrt{\frac{|\varepsilon(\omega)| - \varepsilon'(\omega)}{2}}. \end{aligned} \quad (4)$$

The approximation of the dielectric properties of a thin film by its bulk counterpart starts to fail when the film thickness is of the order of the Fermi wavelength. Quantum confinement effects in metals typically start below ~ 10 nm. A direct DFPT calculation of the dielectric response of Mo_xSi_y thin film slabs is possible, but is not done here. Such slab calculations have been done for Al(111)[26] and Pb(111)[41]. Compared to Al or Pb ($\omega_p \approx 10$ eV), the onset of quantum size effect for Mo_xSi_y ($\omega_p \approx 2$ eV) is expected at smaller film thicknesses.

Since d_{pen} is in most cases much larger than the thickness of the film, multiple reflections inside the film are possible and will alter the absorption of the material in the thin film compared to the bulk form. Therefore, we apply the Transfer Matrix Method (TMM) as implemented in the AbsorptionTMM code [42, 43]. The $n(\omega)$ and $k(\omega)$ enter the TTM as parameters. With the TTM we describe the effect of multiple reflections and the varying incident angle of incoming p -polarized radiation on the absorption of the thin film of thickness d surrounded on the top and bottom by air ($n = 1$). A schematic view of wave propagation in the film is represented in Fig. S2 in SM. The calculated absorption is a function, $A = 1 - T - R$ of the transmission (T) and the reflection (R) of the thin film.

III. RESULTS

Figure 2 shows the atomic structures of the different crystal phases of Mo_xSi_y that are considered in this

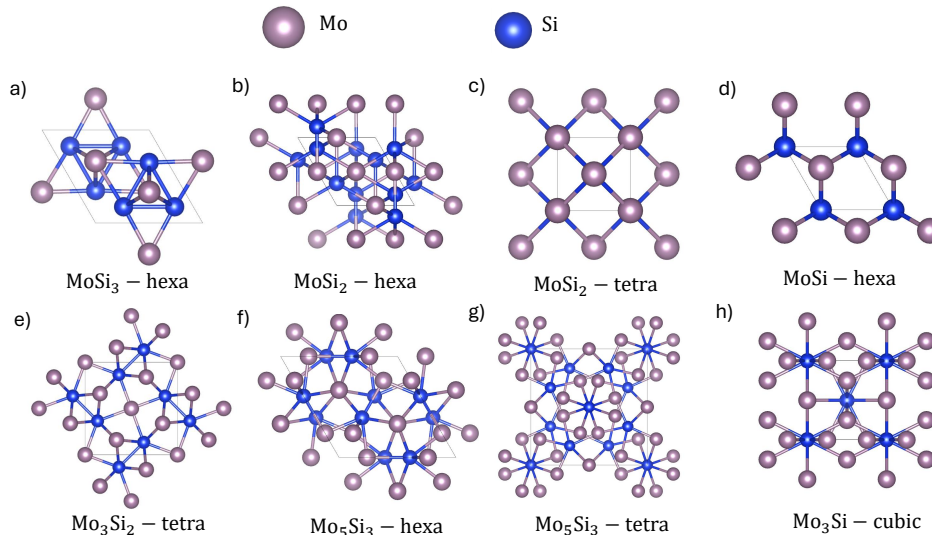


FIG. 2. Overview of the unit cells considered for the different phases of Mo_xSi_y : a) hexagonal MoSi_3 , b) hexagonal MoSi_2 , c) tetragonal MoSi_2 , d) hexagonal MoSi , e) tetragonal Mo_3Si_2 , f) hexagonal Mo_5Si_3 , g) tetragonal Mo_5Si_3 , and h) cubic Mo_3Si .

work. Five experimentally known stable crystal structures are included: MoSi_2 (tetragonal and hexagonal), Mo_5Si_3 (tetragonal and hexagonal), and Mo_3Si (cubic). For both MoSi_2 and Mo_5Si_3 the tetragonal system is the stable low temperature structure, and MoSi_2 is reported to transition to a metastable hexagonal structure around 2173 K [18]. Additionally, we include crystal structures obtained by first-principles simulations [44, 45] that are most likely not thermodynamically stable: MoSi_3 (hexagonal), MoSi (hexagonal), and Mo_3Si_2 (tetragonal), but enable us to study dielectric properties over the stoichiometric range of $0.25 \leq \frac{x}{x+y} \leq 0.75$.

Before simulating the emissivity of Mo_xSi_y in thin-film form, we first examine the electronic structure of the crystals. In Figure 3 (top row), the band structures along high-symmetry lines [46] of the eight crystal structures are shown. We see that all, except for one, of the crystals are metals with a finite density of states (DOS) at the Fermi level (E_F). Only MoSi_2 in the hexagonal phase is a small band-gap semiconductor. In Figure 3 (middle row), the $\text{DOS}(E)$ of the Mo_xSi_y crystals are shown over an energy range ± 2 eV around E_F . A high $\text{DOS}(E_F)$ is an indication that the material is potentially a good metal with high conductivity. In the Drude model, a high $\text{DOS}(E_F)$ can be seen as a high valence electron density ρ_v . This model only describes intra-band electronic screening and links ρ_v to the plasma frequency by $\omega_p = \sqrt{\frac{\rho_v e^2}{\epsilon_0 m}}$, with electron charge e and effective mass m , and vacuum permittivity ϵ_0 . As the imaginary part of the Drude dielectric function Eq. (2) scales with ω_p^2 , the bulk absorption coefficient ($\alpha = \frac{2\omega}{c} k$) is a function of ρ_v through the extinction coefficient $k(\rho_v, \omega)$. We have tabulated the $\text{DOS}(E_F)$ per volume of the unit cell in Table I. The $\text{DOS}(E_F)$ is not the same throughout the

seven metallic systems, therefore, it is expected that the conductivity of the films will vary with Mo_xSi_y stoichiometry, provided that these variations are not exactly compensated by differences in effective mass and relaxation time. Being that Mo carries six valence electrons, and Si only four, one might expect that increasing Mo/Si ratio in a Mo_xSi_y film leads to a higher DOS nearby the E_F . However, for the calculated parameters tabulated in Table I, we do not find a statistically significant correlation (p-value of 0.07) between the stoichiometric ratio and $\text{DOS}(E_F)$, indicating that the electronic properties of Mo_xSi_y films cannot be trivially inferred by stoichiometry only. The influence of the crystal structure is further shown in the following, where we calculate dielectric function, absorption spectrum, the plasma frequency (determined by the curvature of the full band structure around E_F), and emissivity.

TABLE I. Calculated materials parameters of Mo_xSi_y crystals: $\text{DOS}(E_F)/\Omega$ ($1/(\text{eV}\text{\AA}^3)$), static dielectric constant ϵ_∞ , high frequency dielectric constant ϵ_∞ , and Drude plasma frequency ω_p .

$\frac{x}{x+y}$	Crystal	$\text{DOS}(E_F)/\Omega$	ϵ_∞	ω_p (eV)	ϵ_0
0.25	MoSi_3 (hexa)	0.019	512	206	4.17
0.33	MoSi_2 (hexa)		57	290	0.50
0.33	MoSi_2 (tetra)	0.029	76	29	2.83
0.5	MoSi (hexa)	0.027	48	44	3.81
0.60	Mo_3Si_2 (tetra)	0.06	642	177	4.04
0.63	Mo_5Si_3 (hexa)	0.055	339	169	3.11
0.63	Mo_5Si_3 (tetra)	0.06	262	155	3.19
0.75	Mo_3Si (cubic)	0.03	103	96	5.57

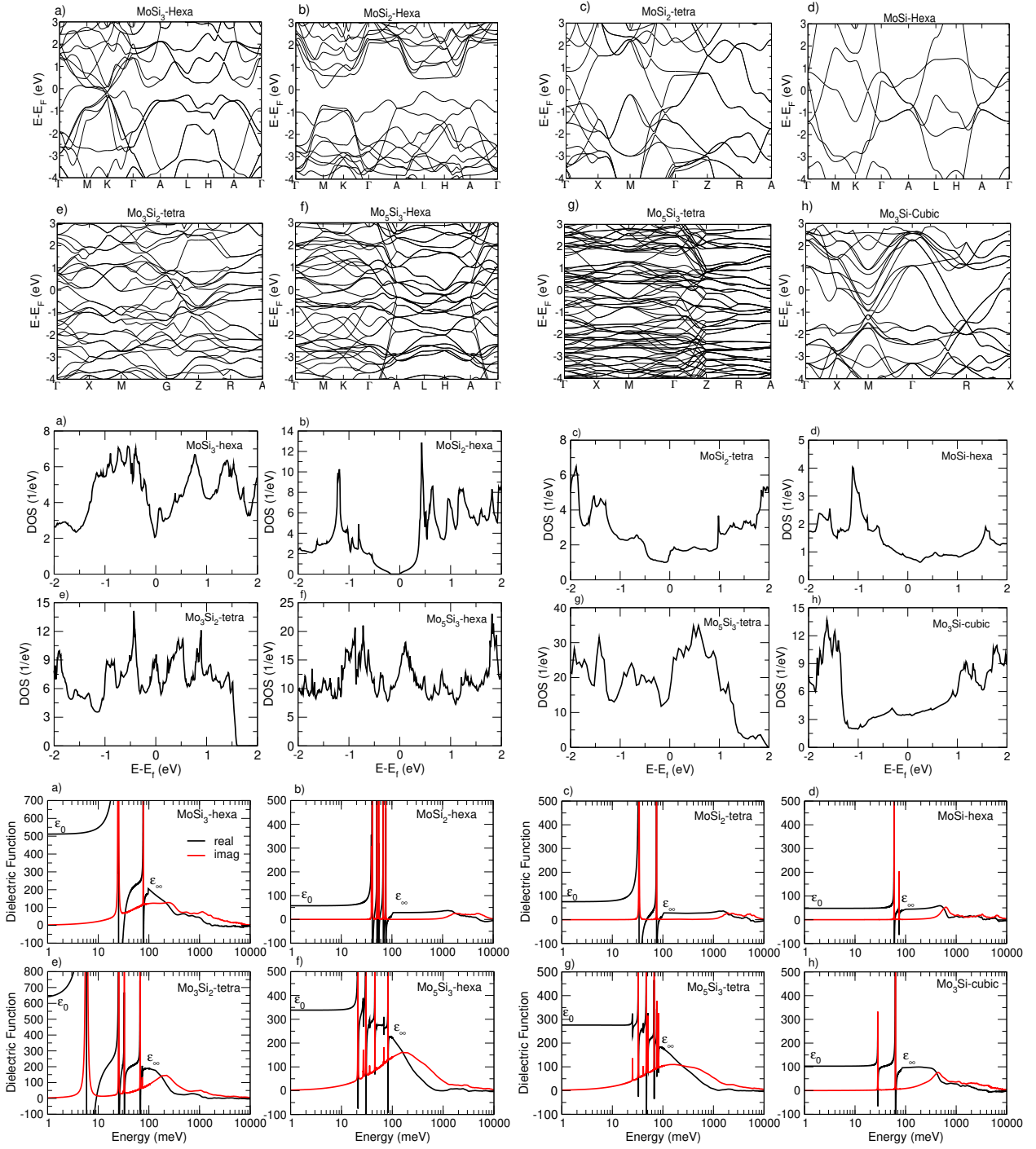


FIG. 3. From top to bottom: Band structure, density of states, and dielectric function of a) hexagonal MoSi_3 , b) hexagonal MoSi_2 , c) tetragonal MoSi_2 , d) hexagonal MoSi , e) tetragonal Mo_3Si_2 , f) hexagonal Mo_5Si_3 , g) tetragonal Mo_5Si_3 , and h) cubic Mo_3Si . The dielectric function is based on electronic inter-band and ionic contributions only. The black/red line denotes the real/imaginary part in $\varepsilon(\omega) = \varepsilon'(\omega) + i\varepsilon''(\omega)$, respectively.

Bulk dielectric function

To calculate optical properties of the materials, we need to calculate the frequency-dependent response of the material to an electric field. Here, we calculate the

dielectric function Eq. (1) of the electronic system and in the ionic lattice, separately. The DFPT calculated dielectric functions, including electronic inter-band and ionic contributions, for all eight Mo_xSi_y crystals are presented in Figure 3 (bottom). The real and imaginary parts of the

dielectric function are colored black and red, respectively. In the high-frequency range only electronic contributions are present, whereas the ionic contributions (here represented by sharp features) dominate below ~ 100 meV. The phonon frequencies of the lattice determine the frequency range of the ionic contributions. Only 'dipole-active' phonon modes have finite oscillator strength and contribute to the dielectric function. Fig. 3 (bottom) shows that the ionic contributions have a sizable effect at low response frequencies, resulting in a static dielectric constant ϵ_0 that is substantially higher than the 'ion-clamped' high frequency dielectric constant ϵ_∞ , see Table I.

The effect of intra-band screening by conduction electrons is approximated with a Drude model. As input for this model, we have used a fixed damping factor $\gamma = 0.15$ eV and calculated the plasma frequency parameter (ω_p) for the eight crystals and tabulated them in the last column of Table I. Compared to ω_p values obtained from fits of the spectra measured in Ref. [5] the here obtained numbers are ~ 3 -4 times higher. We identify two main possible explanations for the large difference. Firstly, the small thickness of the film has a decreasing effect on the effective plasma frequency and an increasing effect on the damping factor as compared to the bulk[47]. Secondly, the lower level of crystallinity of the Mo_xSi_y film grown in the experiment, compared to the perfect crystals in the calculations. Unfortunately, a direct DFT calculation of the plasma frequency of an amorphous or polymorphous structure currently lies (because of the required system size) outside the available computational capabilities. Therefore, we will hereafter present results with and without the intra-band contribution, and analyze the emissivity of a pure Drude thin film over a range of plasma frequencies.

Optical penetration depth & absorption

We have calculated the frequency-dependent penetration depth (d_{pen}) of the eight materials based on only the inter and ion contributions to the bulk dielectric function. It is the length scale after which the intensity of monochromatic light that has entered the material has decayed by a factor of $\frac{1}{e}$. The resulting functions $d_{\text{pen}}(\omega)$ for the eight materials are shown in Figure 4. We find that the film thickness (d) (typically ~ 20 nm) is either $d < d_{\text{pen}}$ or, for some materials, even $d \ll d_{\text{pen}}$ across most of the infrared (IR) spectrum ($\sim 0.01 - 1.7$ eV). This makes the absorption and emission of these materials in thin films different from those of the bulk material. A fraction of the light transmitted through the first air| Mo_xSi_y interface will reflect (internally) at the Mo_xSi_y |air interface, and another fraction will be transmitted. This process repeats itself many times inside the film. Including additional electronic intra-band contributions causes the penetration depth to decrease, as shown in Figure 4 (bottom). Optical absorption is enhanced es-

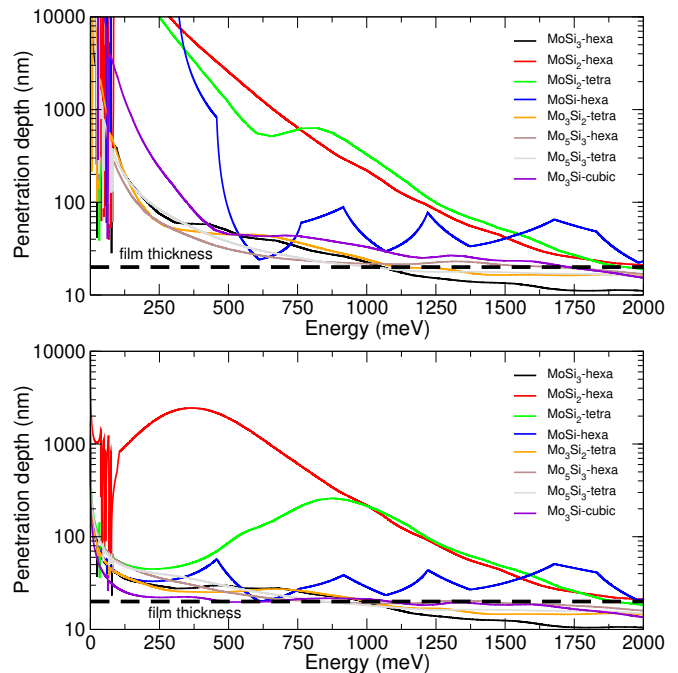


FIG. 4. The frequency-dependent penetration depth of the eight Mo_xSi_y materials based on (*top*) only the inter+ion dielectric function of Fig. 3, and the (*bottom*) full intra+inter+ion dielectric function of Eq. 1) The typical thin film thickness is indicated by the horizontal dashed line.

pecially in the low-frequency range. Still, $d < d_{\text{pen}}$ in the part of the spectrum relevant for emissivity, as we will see when calculating the absorption spectrum. Therefore, the film incorporating all three contributions to the dielectric function should also be regarded as an (optical) thin film. As a consequence, a description of reflection and absorption by a single Fresnel equation at the air| Mo_xSi_y interface will not capture the effect of internal reflections. Therefore, the absorption of the thin film is computed using the TTM method, which accounts for multiple reflections. The computed bulk dielectric function is used as input for the TTM method and results in an absorption $A(\omega, \theta, d)$ that is a function of frequency and incident angle of the light, and film thickness, respectively. For the calculation it is assumed that the film is freestanding, surrounded at the top and bottom by vacuum ($\epsilon = 1$), and that the incoming light is p-polarized and hits the surface under normal incidence $\theta = 90^\circ$. See SM Fig. S2 for a schematic overview.

We will now examine the absorption spectra $A(\omega)$ of a 20 nm thin film under normal incidence angle of two representative materials; one with low penetration depth in the low IR domain, viz. hexagonal Mo_5Si_3 and one with high penetration depth, viz. tetragonal MoSi_2 . The calculated spectra are shown in Figure 5. The three different absorption spectra show the effect of including the different contributions. The for emissivity relevant part of the spectrum, should have overlap with the spectral radiance of a black body. The black body spectrum is

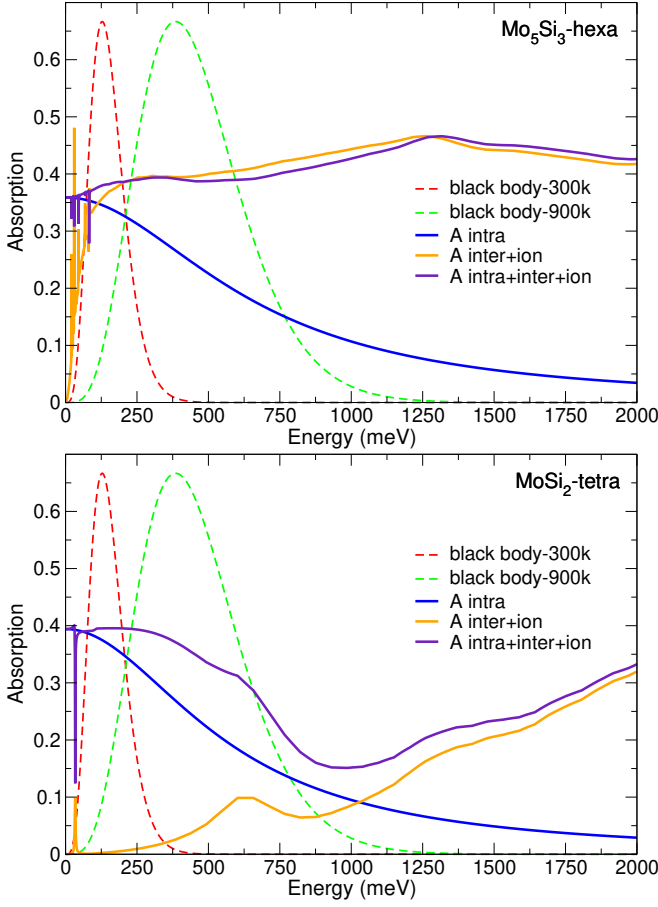


FIG. 5. Absorption spectra for a 20 nm (*top*) hexagonal Mo_5Si_3 and (*bottom*) tetragonal MoSi_2 thin film including different dielectric contributions, and black body radiation spectra at temperatures of 300 K and 900 K. (Black body curves are normalized by peak height.)

described by Planck's law and shown in the two figures for temperatures of 300 and 900 K. By raising the temperature, the black body spectrum covers a different part of the absorption spectra, resulting in a different emissivity. We see that the absorption by intra-band electrons is important at low(er) temperature and becomes less important when the film gets hotter. The contribution of electronic inter-band transitions then starts to dominate. We also see that the overlap with the ionic contributions, i.e. the sharp spikes typically below ~ 50 meV, shows already at 300 K little overlap with the black body spectrum, indicating a minor contribution to the emissivity at this temperature. Comparing the inter+ion spectra to the full intra+inter+ion absorption spectra, we see that for hexagonal Mo_5Si_3 the differences are minor whereas they are large for tetragonal MoSi_2 . This means that uncertainties related to the ω_p , Γ -parameters in the Drude description will have a larger effect on the calculated emissivity for systems such as hexagonal and tetragonal MoSi_2 , but will only play a minor role for the other Mo_xSi_y films. The absorption spectra for the other six

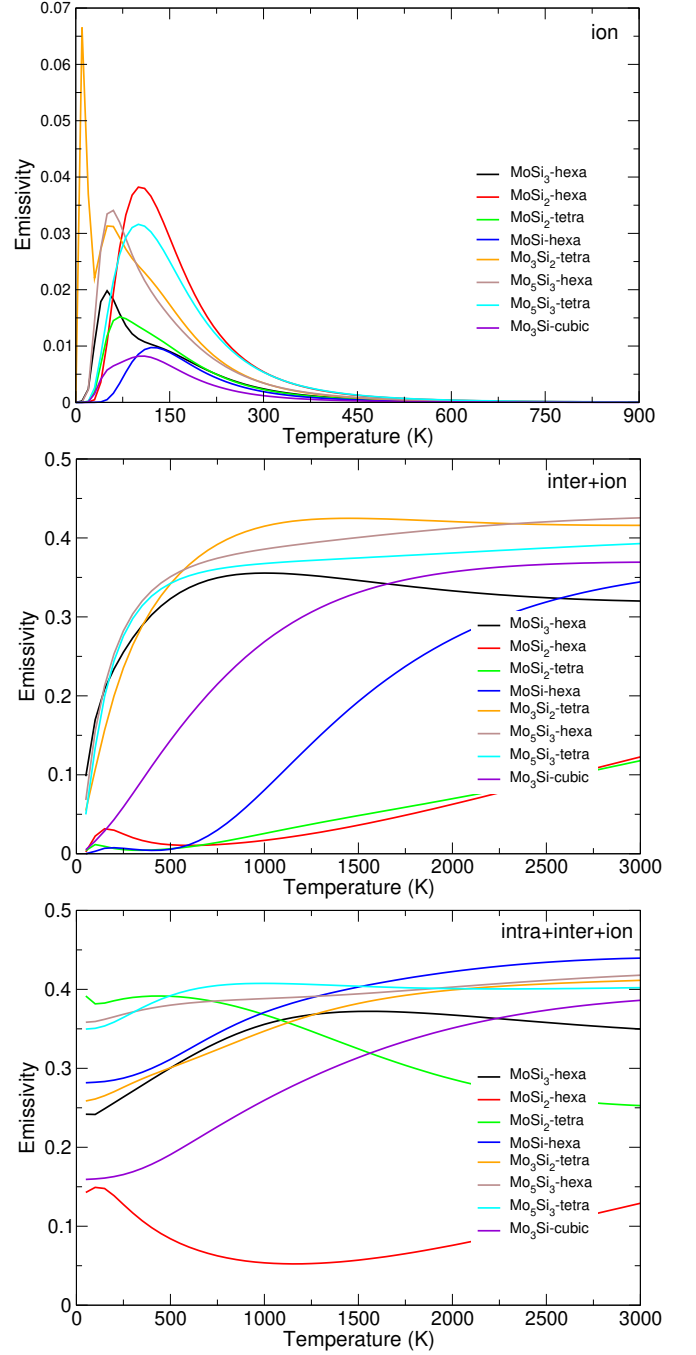


FIG. 6. Temperature dependence of the emissivity of 20 nm thin film Mo_xSi_y based on the (*top*) ionic, (*middle*) inter-band + ionic, and (*bottom*) all three contributions.

Mo_xSi_y stoichiometries are added in the SM (Fig. S4).

Thin film emissivity

The thermal emittance of the Mo_xSi_y crystals in thin film form is quantified by the emissivity:

$$\bar{\varepsilon}(T, \theta) = \frac{\int A(\omega, \theta, d) B(\omega, T) d\omega}{\int B(\omega, T) d\omega}, \quad (5)$$

which is a number between zero and one[48]. Kirchoff's law is applied in Eq. (5), meaning that to maintain the thermal equilibrium of the film, its emissivity is equal to its absorptivity. $B(\omega, T)$ is the spectral radiance of a black body at temperature T . In this setup both the top and bottom surfaces emit the same power. The temperature dependence of the emissivity for all eight crystalline films is shown in Figure 6. The 0 to 3000 K temperature range is evaluated, irrespective of whether the crystal is thermodynamically stable or molten at these temperatures. Note that the figure scales on the y-axes differ, and that the three separate contributions to the dielectric function Eq. (1) are added incrementally (ion, ion+inter, ion+inter+intra) from top to bottom in the three plots.

As discussed in the previous section, the contribution of ionic screening to the emissivity is expected to be low. Therefore, we have calculated the emissivity solely from the ionic contributions and present the results in Figure 6 (top). The contribution of the IR emission from the ionic lattice is indeed low; depending on the material, the lattice contributes between 3 to 10 percent of the total emissivity. Above room temperature (RT), the ionic contribution to the emissivity becomes even negligible. MoSi_2 -hexa forms the exception here, because of its small electronic contribution to emissivity as we will see next. In Figure 6 (middle), the inter-band electronic contributions are added next to the ionic contributions, resulting in an increase of the emissivity by an order of magnitude. For all materials the emissivity increases with temperature to a high value, however, without the intra-band contribution both phases of MoSi_2 show much lower emissivity. In the last Figure 6 (bottom), the intra-band electronic contributions are added as well. This substantially increases the emissivity at low temperatures for all materials, whereas the differences are minor at high temperatures. Surprisingly, the film with the highest emissivity at RT, MoSi_2 -tetra, is the least emissive in Fig. 6 (middle), i.e. without including the intra-band contribution. To understand this, we calculate the emissivity of a pure Drude thin film. Figure 7 shows four Drude emissivity curves; for two typical values of the damping factor (slightly above and below $\gamma = 0.15$) and at 300 and 900 K. We see that intra-band contribution to the thin film emissivity can be substantial and depends sensitively on the plasma frequency. The calculated value of ω_p for MoSi_2 -tetra (see Table I) lies close to the peak emissivity. We note that this emissivity is already close to the theoretical maximum of 0.5, determined by the absorption of a thin film in air occurring when $n = k$ [49]. The increase around RT for MoSi_2 -hexa is the result of a small finite ω_p value, which

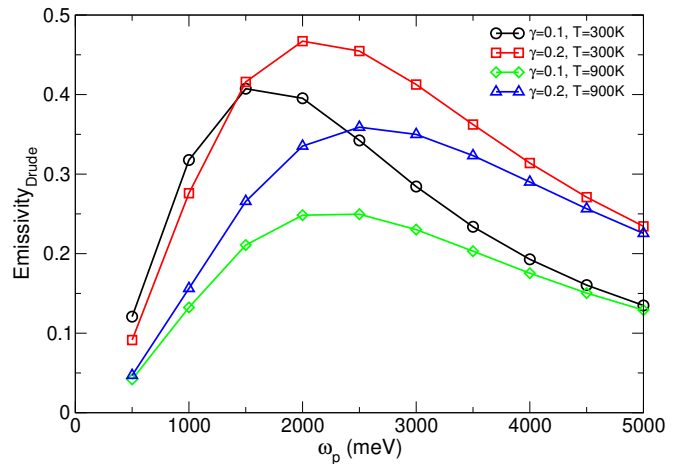


FIG. 7. Emissivity of a 20 nm Drude thin film in which the intra-band electronic excitations are parameterized by the plasma frequency (ω_p) and a damping factor (γ).

is a more valid approximation in the high temperature regime. Given that we compute a bandgap of 0.2 eV, $\omega_p = 0$, i.e. no intra-band contribution would be a better approximation at RT. Summarizing, we can conclude that the emissivity in Mo_xSi_y films predominantly arises from electronic contributions to the dielectric function, and that they do not show a simple (linear) relation with the stoichiometric ratio.

Film thickness is an important parameter for the emissivity of thin films. Figure 8 shows how the emissivity of Mo_xSi_y films changes with thickness. Here, the temperature is set to 900 K. As the thickness of the film decreases from 40 nm, the emissivity increases for all Mo_xSi_y films, with the exception of hexagonal MoSi_2 . The emissivity reaches its maximum around ~ 10 nm. Beyond this point, as the thickness continues to decrease from 10 to 0 nm, the emissivity decreases. Including the intra-band contributions lowers the thickness of the peak maximum to ~ 5 -10 nm depending on the crystal phase. As seen before, MoSi_2 stands out from the other films. The difference is related to the presence of a band gap (hexagonal) and low DOS around E_F (tetragonal), resulting in almost no inter-band contributions at low frequency.

Films with reduced crystallinity

Up to this point, all calculations were based on the crystals depicted in Fig. 2. Conventional techniques to grow Mo_xSi_y thin films are based on physical or chemical vapor deposition. Since it is known that these techniques do not produce a perfect crystal structure in the entire film unless special care is taken to control growth (i.e. control of substrate temperature, deposition parameters and precursor materials), even after thermal annealing[5], we study the influence of imperfections in the crystal on the calculated emission coefficient. Here, we select

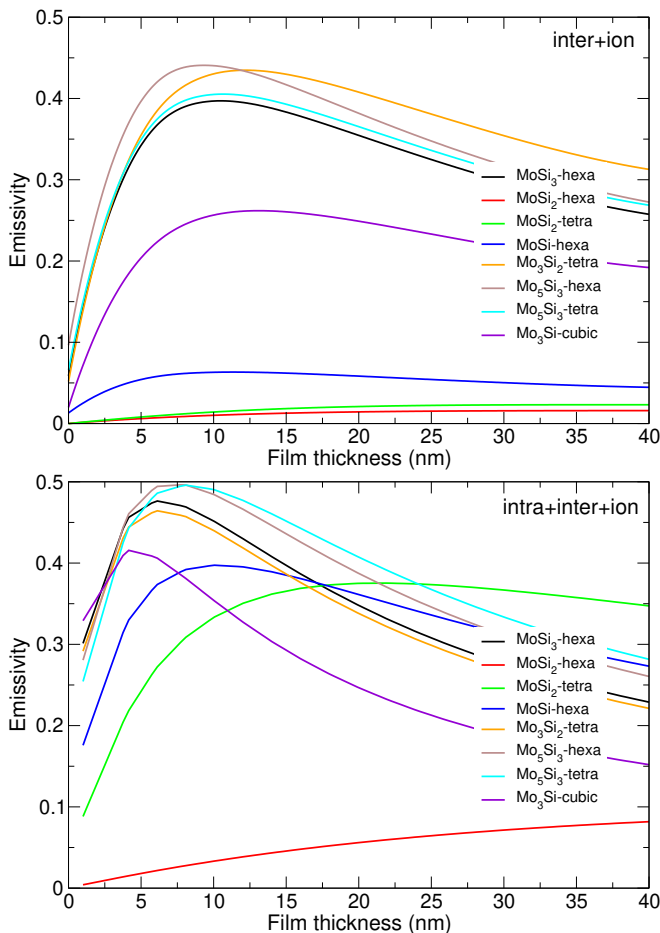


FIG. 8. Thickness dependence the emissivity of Mo_xSi_y thin films at 900 K based on (*top*) inter-band and ionic contributions, and based on (*bottom*) all three contributions.

tetragonal- MoSi_2 to investigate the influence of defects in the crystal on a qualitative level. This stoichiometry ($1/3$) is most frequently appearing in the literature and, as we have seen, has the peculiar property of low inter-band and high intra-band contribution to the emissivity. As a test cell, we construct a $3 \times 3 \times 3$ supercell and consider two kinds of defects: *i*) *Mo-defected*: one additional Mo atom replacing a randomly chosen Si atom in the supercell, and *ii*) *Mo&Si-swapping*: interchanging the position of one Si and one Mo in the supercell. The crystal volume and the atomic coordinates are retained. For the two test cells and for the perfect structure in this supercell, we calculate inter and ion contributions to the dielectric function. The resulting $\epsilon(\omega)$ are compared to the perfect crystal in Figures 9 a,b). The defected crystals show a substantial increase of absorption/emission strength in the IR part of the spectrum. This is the result of a stronger response in the energy window between ~ 100 and 700 meV in the dielectric function. In Fig. 9 c), we see that the DOS in this frequency range (centered around E_F) of the defected systems is larger. Apparently, these states participate in the increase of

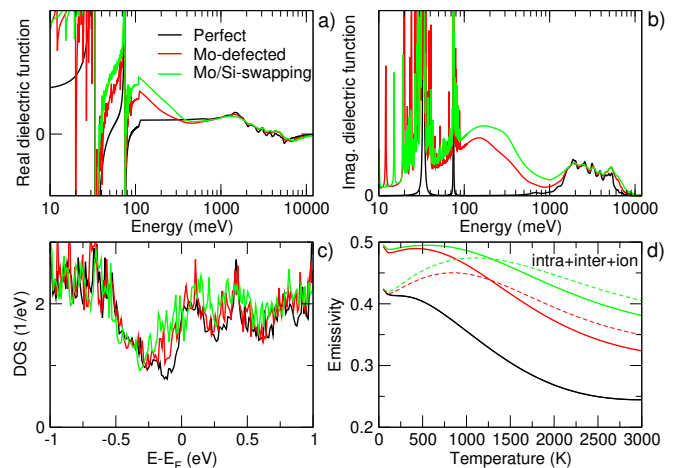


FIG. 9. Comparison between perfect (black line) and defected (red & green lines) tetragonal MoSi_2 . a) Real part and b) imaginary part of inter-ion dielectric function, c) density of states, and d) intra+inter-ion emissivity versus temperature. Dashed lines in d) are the calculated emissivities using the same ω_p value for all three systems.

the amount and dipole-activity of inter-band transitions in the IR regime. The effective ionic contribution to the emissivity is largely unchanged, except for the broadening of the two peaks below 100 meV (see Fig. 9 b). To study the intra-band contributions, we have calculated the plasma frequencies for the Mo-defected and Mo&Si-swapping test systems as 1.83 and 1.66 eV, respectively. These values are lower than the plasma frequency of the perfect crystal (2.58 eV in supercell). This is to be expected, as the defects break crystal symmetry and add more localized (dispersion-less) electronic states into the band structure. We refer to the SM for the relation between ω_p and the electronic band dispersion. As a result of increased inter-band transitions and decreased ω_p values, the emissivity in both types of defected tetragonal MoSi_2 films increases drastically with respect to the perfect crystalline film. Figure 9 d) shows that this increase is expected to raise the emissivity throughout the here studied temperature range. The dashed lines correspond to the emissivity calculated for the case of same the ω_p value (that of the perfect system) used also for the defected systems. This shows that the emissivity increase at low temperature is mainly attributed to the decrease of the plasma frequency, but the increase around ~ 1000 K is mainly originating from the increased inter-band transitions. These results indicate that high emissivity for a thin film of MoSi_2 most likely means that the atomic structure in the film is defected or partially amorphous.

IV. DISCUSSION

In this computational work, we have mainly studied Mo_xSi_y thin films in highly symmetric crystalline form,

whereas in experimentally grown thin films there is normally disorder and microstructure. Therefore, the observables reported here should be used as qualitative guidelines and trends, rather than quantitative predictions on the effects of stoichiometric change. For example, the calculated 900 K emissivity for 20 nm thin films of MoSi₂ (tetragonal) is 0.37, which is in qualitative agreement with experimental thin film emissivity of 0.33 in Ref. [5]. Also in agreement with experiment, our calculations show a reduced thin film emissivity in the hexagonal crystal phase. We attribute the larger emissivity in the tetragonal as compared to the hexagonal phase, to the closing of the band gap and the resulting sharp increase in the Drude plasma frequency. We note that the calculated thin film emissivity of hexagonal MoSi₂ of 0.06 is significantly lower than the experimental value of 0.28. This difference is related to the nanoscale morphology of the film and the presence of defects.

The emissivity of the thin film can be improved by changing the the Mo_xSi_y stoichiometry. Surprisingly, when the aim is high emissivity films with MoSi₂ stoichiometry, we find that one should not focus on the growth of the most perfect crystalline thin film. Rather, our calculations on defected test systems demonstrate increased dipolar activity in the IR part of the dielectric spectrum. We note that during the annealing process of the experimental thin films, the amorphous parts of the film become more crystalline as demonstrated by sharpening of the XRD diffraction spectrum[5]. Thereby, annealing of the film probably results in a system with crystalline domains with embedded defects and amorphous parts, i.e. more comparable to the test systems used here. The notable improvement in the emissivity of the defected tetragonal-MoSi₂ test system arises in part from an increased contribution of inter-band transitions in the ~ 100 -700 meV window. These calculations only qualitatively demonstrate this effect, a follow up study is needed to determine how representative these test systems are, by calculating the likeliness/energetics of defect formation. We have checked that the effect of increased IR absorption is retained also after structural relaxation of the test systems, be it with somewhat lowered oscillator strength. The corresponding dielectric functions have been added to the SM. We note that this is a truly electronic effect and is not related to a change of thin film morphology. For example, an explanation based on an increase in surface roughness and its effect on the film's emissivity[50] would not fit the model setup chosen here. We furthermore note that, in general, defects do not always increase the emissivity of a semiconductor. Ref. [51] presents a study of SiO₂ and ZrO₂ in presence of oxygen vacancies. The study shows that if defects introduce mid-gap states, the emissivity increases (ZrO₂), but if it introduces empty states in the conduction bands, the emissivity decreases (SiO₂).

Lastly, we would like to discuss two limitations of the applied computational setup. First, the fixed Gaussian smearing level used for all materials results in a small

artifact intra-band contribution for MoSi₂-hexa. DFT calculations show a small band gap of 0.2 eV, therefore, at 0 K one expects a semiconductor behavior without intra-band contribution, i.e. $\omega_p = 0$. However, at elevated temperatures, thermal excitations of the electrons can make the material partially metallic. Determining the temperature dependence of the plasma frequency by specific Fermi-Dirac broadening would be an interesting next step. Second, by approximating the dielectric properties of the thin films by their bulk counterpart, the calculated emissivity values for ultra-thin films, ie. below ~ 5 nm have less predictive value as compared to thicker films. This suggests that the slope of the $\bar{\epsilon}(T)$ curve in the 0 to 5 nm range of Figure 8 is likely subject to error. In future work, the exact impact of the QSE and of surface reconstruction on the dielectric function can be evaluated through DFPT slab calculations.

V. CONCLUSION

We have calculated the electronic and dielectric properties of different phases of bulk Mo_xSi_y crystals using a method based on first-principles. Our findings highlight the significant changes in the dielectric function due to variations in stoichiometry and crystal structure. The calculated frequency-dependent dielectric functions serve as input for further calculations of the optical absorption of thin films. The predicted optical penetration depths are generally larger than the typical thin film thickness of 20 nm, therefore the effect of multiple internal reflections has been included in the calculated absorption. For crystals with high metallicity, such as Mo₅Si₃, Mo₃Si₂, Mo₃Si, and MoSi₃, we find a broad absorption window in the IR window originating from electronic inter- and intra-band contributions. In contrast, compositions such as MoSi₂ and MoSi have a much lower inter-band contribution to absorption. This affects their emissivity and, therefore, limit possible high-temperature applications.

For all eight considered Mo_xSi_y materials, we have calculated the emissivity of a thin film as function of temperature. The emissivity shows a complex relation as a function of stoichiometry, which cannot simply be described by the Mo content. In line with experiments of Ref. [5], we find an increase of the emissivity by changing the crystal phase from hexagonal to tetragonal in a 20 nm thin MoSi₂ film at 900 K. The calculated emissivities are in qualitative agreement with these experiments, predicting an emissivity of 0.37 for a 20 nm tetragonal MoSi₂ film at 900 K, compared to ~ 0.33 in experiment. We demonstrate that ionic contributions have only a small effect on emission at room temperature and become negligible at higher temperatures. Furthermore, our calculations show that atomic defects in MoSi₂ introduce states close to the Fermi level, resulting in increased inter-band absorption and a reduction in the intra-band Drude plasma frequency. Together, these effects increase the emissivity of defective MoSi₂ relative to perfect tetragonal MoSi₂.

We have determined that the thickness of the Mo_xSi_y film is a crucial factor for high emissivity. The highest emissivity coefficient is predicted for Mo_5Si_3 , Mo_3Si_2 and MoSi_3 thin films with a thickness between 5 and 10 nm. These findings may be useful for the development of applications that require high transmission of short-wave light, by guiding Mo_xSi_y growth strategies that lead to thin films with an increased emission coefficient and an

optimal film thickness.

VI. ACKNOWLEDGMENT

This work was jointly funded by the Dutch Ministry of Economic Affairs and ASML within the framework of the TKI-HTSM program, project 2212P21 EMOSION. ZG gratefully acknowledges the support of Fedor Akhmetov for assistance with setting up the TMM absorption calculations.

-
- [1] X. Zhang, Y. Chen, and J. Hu, Recent advances in the development of aerospace materials, *Progress in Aerospace Sciences* **97**, 22 (2018).
- [2] M. Werner and W. Fahrner, Review on materials, micro-sensors, systems and devices for high-temperature and harsh-environment applications, *IEEE Transactions on Industrial Electronics* **48**, 249 (2001).
- [3] K. Pan, Y. Yang, S. Wei, H. Wu, Z. Dong, Y. Wu, S. Wang, L. Zhang, J. Lin, and X. Mao, Oxidation behavior of mo-si-b alloys at medium-to-high temperatures, *Journal of Materials Science and Technology* **60**, 113 (2021).
- [4] S. Edalatpour and M. Francoeur, Size effect on the emissivity of thin films, *Journal of Quantitative Spectroscopy and Radiative Transfer* **118**, 75 (2013).
- [5] A. Baskakov, R. van de Kruijs, Z. S. Houweling, G. Colombi, F. Akhmetov, J. M. Sturm, and M. Ackermann, Relation between electronic structure and emissivity of mosi2-based thin membranes for radiative cooling, *Journal of Alloys and Compounds* **1018**, 179277 (2025).
- [6] A. Merchant, S. Batzner, S. S. Schoenholz, M. Aykol, G. Cheon, and E. D. Cubuk, Scaling deep learning for materials discovery, *Nature* **624**, 80 (2023).
- [7] A. Jain, S. P. Ong, G. Hautier, W. Chen, W. D. Richards, S. Dacek, S. Cholia, D. Gunter, D. Skinner, G. Ceder, *et al.*, Commentary: The materials project: A materials genome approach to accelerating materials innovation, *APL materials* **1**, 10.1063/1.4812323 (2013).
- [8] E. A. Brandes and G. Brook, *Smithells metals reference book* (Elsevier, 2013).
- [9] Z. Yao, J. Stiglich, and T. Sudarshan, Molybdenum silicide based materials and their properties, *Journal of Materials Engineering and Performance* **8**, 291 (1999).
- [10] A. K. Czerny, W. Ma, C. S. Hausner, P. Franke, M. Rohde, and H. J. Seifert, Thermodynamic assessment of the mo-si system, *Advanced Engineering Materials* **26**, 2302085 (2024).
- [11] A. Vasudévan and J. Petrovic, A comparative overview of molybdenum disilicide composites, *Materials Science and Engineering: A* **155**, 1 (1992), proceedings of the First High Temperature Structural Silicides Workshop.
- [12] T. Dasgupta and A. Umarji, Improved ductility and oxidation resistance in nb and al co-substituted mosi2, *Intermetallics* **16**, 739 (2008).
- [13] A. Bahr, S. Richter, R. Hahn, T. Wojcik, M. Podsednik, A. Limbeck, J. Ramm, O. Hunold, S. Kolozsvári, and H. Riedl, Oxidation behaviour and mechanical properties of sputter-deposited tmsi2 coatings (tm = mo, ta, nb), *Journal of Alloys and Compounds* **931**, 167532 (2023).
- [14] K. Kumar and C. Liu, Ordered intermetallic alloys, part ii: silicides, trialuminides, and others, *JOM* **45**, 28 (1993).
- [15] S. Weis, T. Uhlig, G. Wagner, T. Lampke, W. Bauer, and A. Moldenhauer, High-temperature corrosion and radiation characteristics of thermal sprayed molybdenum disilicide-based coatings, *IOP Conference Series: Materials Science and Engineering* **118**, 012007 (2016).
- [16] X. Tao, Z. Liang, J. Li, J. Zhang, X. Guo, and M. Wang, Anti-oxidation of emitting agents in tasi2-mosi2-borosilicate glass high emissivity coating, *Ceramics International* **48**, 37333 (2022).
- [17] X. Yang, Y. Wan, J. Li, J. Liu, M. Wang, and X. Tao, High emissivity mosi2-sic-al2o3 coating on rigid insulation tiles with enhanced thermal protection performance, *Materials* **17**, 10.3390/ma17010220 (2024).
- [18] A. B. Gokhale and G. J. Abbaschian, The mo-si (molybdenum-silicon) system, *Journal of Phase Equilibria* **12**, 493 (1991).
- [19] J. Hawk and D. Alman, A comparative study of the abrasive wear behavior of mosi2, *Scripta Metallurgica et Materialia* **32**, 725 (1995).
- [20] M. Choi, C. Park, and J. Hong, Development and optimization of metal silicide euv pellicle for 400w euv lithography, *Nanotechnology* **36**, 06LT01 (2024).
- [21] M. Choi and J. Hong, Composition-dependent properties of ultra-thin mosix based extreme ultraviolet pellicle, *Nanotechnology* **36**, 22LT01 (2025).
- [22] M. Liton, M. Helal, M. Khan, M. Kamruzzaman, and A. Farid Ul Islam, Mechanical and opto-electronic properties of α -mosi2: a dft scheme with hydrostatic pressure, *Indian Journal of Physics* **96**, 4155 (2022).
- [23] J.-Q. Zheng, J. Chen, B.-H. Zhang, X.-J. Liu, Z.-M. Chen, H.-B. Wu, and Z.-R. Huang, Electrical percolation and infrared emissivity of pressureless sintered sic-mosi2 composites tailored by sintering temperature, *Journal of the European Ceramic Society* **39**, 3981 (2019).
- [24] M. J. van Setten, S. Er, G. Brocks, R. A. de Groot, and G. A. de Wijs, First-principles study of the optical properties of $\text{mg}_x\text{ti}_{1-x}\text{h}_2$, *Phys. Rev. B* **79**, 125117 (2009).
- [25] Z.-Y. Jiao, S.-H. Ma, and J.-F. Yang, A comparison of the electronic and optical properties of zinc-blende, rocksalt and wurtzite aln: A dft study, *Solid State Sciences* **13**, 331 (2011).

- [26] W. Ming, S. Blair, and F. Liu, Quantum size effect on dielectric function of ultrathin metal film: a first-principles study of al 111, *Journal of Physics: Condensed Matter* **26**, 505302 (2014).
- [27] H. Xiang, F. Dai, and Y. Zhou, Secrets of high thermal emission of transition metal disilicides tmsi2 (tm=ta, mo), *Journal of Materials Science and Technology* **89**, 114 (2021).
- [28] J. Song, Y. Cheng, H. Xiang, F.-Z. Dai, S. Dong, G. Chen, P. Hu, X. Zhang, W. Han, and Y. Zhou, Medium and high-entropy transition metal disilicides with improved infrared emissivity for thermal protection applications, *J. Mat. Sci. & Tech.* **136**, 149 (2023).
- [29] P. E. Blöchl, Projector augmented-wave method, *Phys. Rev. B* **50**, 17953 (1994).
- [30] G. Kresse and J. Hafner, Ab-initio molecular-dynamics for liquid-metals, *Phys. Rev. B* **47**, 558 (1993).
- [31] G. Kresse and J. Furthmüller, Efficient iterative schemes for ab initio total-energy calculations using a plane-wave basis set, *Phys. Rev. B* **54**, 11169 (1996).
- [32] G. Kresse and D. Joubert, From ultrasoft pseudopotentials to the projector augmented-wave method, *Phys. Rev. B* **59**, 1758 (1999).
- [33] J. P. Perdew, A. Ruzsinszky, G. I. Csonka, O. A. Vydrov, G. E. Scuseria, L. A. Constantin, X. Zhou, and K. Burke, Restoring the density-gradient expansion for exchange in solids and surfaces, *Phys. Rev. Lett.* **100**, 136406 (2008).
- [34] X. Gonze and C. Lee, Dynamical matrices, born effective charges, dielectric permittivity tensors, and interatomic force constants from density-functional perturbation theory, *Phys. Rev. B* **55**, 10355 (1997).
- [35] X. Wu, D. Vanderbilt, and D. R. Hamann, Systematic treatment of displacements, strains, and electric fields in density-functional perturbation theory, *Phys. Rev. B* **72**, 035105 (2005).
- [36] M. Gajdoš, K. Hummer, G. Kresse, J. Furthmüller, and F. Bechstedt, Linear optical properties in the projector-augmented wave methodology, *Phys. Rev. B* **73**, 045112 (2006).
- [37] K.-H. Lee and K. J. Chang, First-principles study of the optical properties and the dielectric response of al, *Phys. Rev. B* **49**, 2362 (1994).
- [38] J. Harl, G. Kresse, L. D. Sun, M. Hohage, and P. Zeppenfeld, Ab initio reflectance difference spectra of the bare and adsorbate covered cu(110) surfaces, *Phys. Rev. B* **76**, 035436 (2007).
- [39] See Supplemental Material at <http://link.aps.org/supplemental/10.1103/6v8t-117b> for supporting information about the calculations, which includes Ref. [52].
- [40] M. Bokdam, T. Sander, A. Stroppa, S. Picozzi, D. D. Sarma, C. Franchini, and G. Kresse, Role of polar phonons in the photo excited state of metal halide perovskites, *Sci. Rep.* **6**, 28618 (2016).
- [41] X. Zubizarreta, E. V. Chulkov, I. P. Chernov, A. S. Vasenko, I. Aldazabal, and V. M. Silkin, Quantum-size effects in the loss function of pb(111) thin films: An ab initio study, *Phys. Rev. B* **95**, 235405 (2017).
- [42] S. J. Byrnes, Multilayer optical calculations (2020), [arXiv:1603.02720](https://arxiv.org/abs/1603.02720) [physics.comp-ph].
- [43] AbsorptionTMM, <https://github.com/udcm-su/AbsorptionTMM>, accessed: 2024-08-10.
- [44] Materials data on si3mo by materials project [10.17188/1315941](https://materialsproject.org/materials/10.17188/1315941) (2020).
- [45] R. Woods-Robinson, Y. Xiong, J.-X. Shen, N. Winner, M. K. Horton, M. Asta, A. M. Ganose, G. Hautier, and K. A. Persson, Designing transparent conductors using forbidden optical transitions, *Matter* **6**, 3021 (2023).
- [46] W. Setyawan and S. Curtarolo, High-throughput electronic band structure calculations: Challenges and tools, *Computational Materials Science* **49**, 299 (2010).
- [47] D. Shah, M. Yang, Z. Kudyshev, X. Xu, V. M. Shalaev, I. V. Bondarev, and A. Boltasseva, Thickness-dependent drude plasma frequency in transdimensional plasmonic tin, *Nano Lett.* **22**, 4622 (2022).
- [48] R. Siegel, *Thermal Radiation Heat Transfer* (CRC Press, 2001).
- [49] L. N. Hadley and D. M. Dennison, Reflection and transmission interference filters part i. theory, *J. Opt. Soc. Am.* **37**, 451 (1947).
- [50] I. Simonsen, Optics of surface disordered systems, *The European Physical Journal Special Topics* **181**, 1 (2010).
- [51] S. M. Avdoshenko and A. Strachan, High-temperature emissivity of silica, zirconia and samaria from ab initio simulations: role of defects and disorder, *Modelling and Simulation in Materials Science and Engineering* **22**, 075004 (2014).
- [52] J. Harl, *The linear response function in density functional theory*, *Ph.D. thesis*, University of Vienna, Austria (2008).